

First data from DM-Ice17

J. Cherwinka,¹ D. Grant,² F. Halzen,³ K.M. Heeger,⁴ L. Hsu,⁵ A.J.F. Hubbard,^{3,4} A. Karle,³
M. Kauer,^{3,4} V.A. Kudryavtsev,⁶ C. Macdonald,⁶ R.H. Maruyama,^{4,*} S. Paling,⁷ W. Pettus,^{3,4}
Z.P. Pierpoint,^{3,4} B.N. Reilly,^{3,4,†} M. Robinson,⁶ P. Sandstrom,³ N.J.C. Spooner,⁶ S. Telfer,⁶ and L. Yang⁸

(The DM-Ice Collaboration)

¹*Physical Sciences Laboratory, University of Wisconsin-Madison, Stoughton, WI 53589, USA*

²*Department of Physics, University of Alberta, Edmonton, Alberta, Canada*

³*Department of Physics and Wisconsin IceCube Particle Astrophysics Center,
University of Wisconsin-Madison, Madison, WI 53706, USA*

⁴*Department of Physics, Yale University, New Haven, CT 06520, USA*

⁵*Fermi National Accelerator Laboratory, Batavia, IL 60510, USA*

⁶*Department of Physics and Astronomy, University of Sheffield, Sheffield, UK*

⁷*STFC Boulby Underground Science Facility, Boulby Mine, Cleveland, UK*

⁸*Department of Physics, University of Illinois at Urbana-Champaign, Urbana, IL 61801, USA*

(Dated: 10 November 2014)

We report the first analysis of background data from DM-Ice17, a direct-detection dark matter experiment consisting of 17 kg of NaI(Tl) target material. It was codeployed with IceCube 2457 m deep in the South Pole glacial ice in December 2010 and is the first such detector operating in the Southern Hemisphere. The background rate in the 6.5–8.0 keV_{ee} region is measured to be 7.9 ± 0.4 counts/day/keV/kg. This is consistent with the expected background from the detector assemblies with negligible contributions from the surrounding ice. The successful deployment and operation of DM-Ice17 establishes the South Pole ice as a viable location for future underground, low-background experiments in the Southern Hemisphere. The detector assembly and deployment are described here, as well as the analysis of the DM-Ice17 backgrounds based on data from the first two years of operation after commissioning, July 2011–June 2013.

PACS numbers: 95.35.+d, 29.40.Mc, 95.55.Vj

Keywords: dark matter, DM-Ice, sodium iodide, direct detection, annual modulation, South Pole

I. INTRODUCTION

Astrophysical and cosmological observations suggest that roughly 27% of the Universe is cold dark matter [1]. Although evidence for dark matter has been firmly established [2, 3], its composition and characteristics remain largely unknown. Weakly interacting massive particles (WIMPs) are theoretically favored because they can be produced in the early universe with the correct abundance to result in the observed relic density [4]. A suite of direct detection experiments is now underway [5] to search for WIMPs through observation of WIMP-nucleon scattering [6, 7].

We report on the performance of DM-Ice17, a NaI(Tl) direct dark matter detector deployed at the South Pole in December 2010. DM-Ice17 is designed to demonstrate the feasibility of operating a remote low-background NaI experiment to directly test the annual modulation of the WIMP-nucleon scattering rate observed by DAMA. The expected annual modulation arises from the motion of Earth around the Sun while the Solar System moves through the dark matter halo of our Galaxy [8, 9]. The DAMA/NaI [10] and DAMA/LIBRA [11] experiments,

running at the Laboratori Nazionali del Gran Sasso for a combined 14-year period, have measured a consistent annual modulation at 9.3σ , which they attribute to dark matter. More recently the CoGeNT [12, 13], CRESST [14], and CDMS-II(Si) [15] experiments have observed events in excess of the known backgrounds in their respective detectors. Under the assumption of elastic scattering of WIMPs, these results are inconsistent with exclusion limits set by several direct detection experiments for both spin-independent [16–20] and spin-dependent scattering [20–24]. New dark matter candidates [25–28], instrumentation effects [29, 30], backgrounds [31–33] and modifications on the distributions of the local dark matter halo [34, 35] have all been proposed in an attempt to reconcile these seemingly contradictory results with limited success.

A large radio-pure array of NaI(Tl) crystals placed deep in the Antarctic ice near the South Pole will have the ability to directly test DAMA’s claim [36]. The expected dark matter modulation has a constant phase everywhere on Earth, whereas any modulation resulting from seasonal effects reverses its phase between the Northern and Southern Hemispheres. The South Pole ice offers up to 2800 m of overburden, is extremely radio-pure, and strongly suppresses the effects of environmental and seasonal variations such as temperature, humidity, and pressure. Furthermore, the Amundson-Scott South Pole Station and IceCube Neutrino Detector provide technical

* Corresponding author: reina.maruyama@yale.edu

† Present address: Physics Department, University of Wisconsin-Fox Valley, Menasha, WI, USA

infrastructure and muon coincidence capabilities [37].

II. EXPERIMENTAL SETUP

A. Detector

DM-Ice17 consists of two 8.47 kg NaI(Tl) scintillating crystals; each crystal is optically coupled to two photomultiplier tubes (PMTs) through quartz light guides (see Fig. 1). Each detector assembly (denoted Det-1 and Det-2), along with its data acquisition and control electronics (see Sec. II B), is housed in its own stainless steel pressure vessel and encased in the South Pole ice at a depth of 2457 m (see Sec. II C). The NaI(Tl) crystals, light guides, and photomultiplier tubes are those used by the former NaIAD experiment that ran from 2000–2003 at the Boulby Underground Laboratory [38, 39]. They were stored in sealed copper boxes at the Boulby Underground Laboratory from 2003–2010, when they were retrieved to be used in DM-Ice17.

The two NaI(Tl) crystals, denoted DM80 (Det-1) and DM81 (Det-2) in NaIAD publications, were produced by Bicron and encapsulated by Saint-Gobain. Previously measured background rates at 6–7 keV_{ee} of 7–10 counts/day/keV/kg [38, 39] are consistent with those observed in DM-Ice17 and reported in this paper (see Sec. V). These crystals provide well characterized detectors for this experiment; however, the high background rates limit the sensitivity of DM-Ice17.

Each cylindrical crystal measures 14.0 cm in diameter and 15.0 cm in length. For diffusive light reflec-

tion, the crystals are wrapped in thin sheets of polytetrafluoroethylene (PTFE). They are encapsulated with an oxygen-free high thermal conductivity (OFHC) copper housing and a thin quartz window on either end to protect the hygroscopic crystal. The encapsulation has an outer diameter of 14.6 cm and length of 16.5 cm.

The scintillation light is recorded by 5-inch 9390-UKB PMTs with C636-KFP voltage divider bases (Electron Tubes Limited). The crystals are shielded from the radioactivity in the PMTs with 5.0 cm thick quartz light guides. A 3 mm layer of Q900 silicone gel (Quantum Silicones) coated in EJ-550 optical grease (Eljen Technology) provides optical coupling between the interfaces of the PMTs, light guides, and NaI(Tl) crystals. The gel also helped suppress mechanical shock between components during shipping and deployment. Q900, used in IceCube to couple the PMTs to the pressure housings, has been demonstrated to be robust, clean, and stable for long-term operation at the South Pole.

PTFE tubes (Applied Plastics Technology) around the crystal, light guides, and PMTs serve to reflect light and provide mechanical support against lateral movements. A PTFE disk around the base of each PMT maintains the alignment while Buna-N O-rings on the PTFE tubes and disks hold the detector centered in the pressure vessel. The optical components are both compressed together and protected from mechanical shocks by a series of springs supported by six threaded OFHC copper rods.

The detector assembly is suspended from an OFHC copper plate (orange in Fig. 1 left) which in turn hangs from a stainless steel midplate (gray in Fig. 1 left). Holes for the wires were drilled at 45° through the steel midplate to avoid direct line of sight to the optical components. The lower pressure vessel volume was flushed with dry nitrogen and the holes were potted with silicone-based epoxy; this sealed off the sensitive detector from the upper pressure vessel volume housing the electronics boards (see Sec. II B). A stainless steel cylinder (dark blue in Fig. 1) supports the electronics boards and adds mechanical strength to the top surface of the pressure vessel by transferring some of the load onto the midplate.

Each detector is housed in a stainless steel pressure vessel designed to withstand 10000 psi of external pressure. Pressure spikes exceeding 7000 psi have been observed by IceCube as the drill water column freezes (see Sec. II C). SANMAC SAF 2205 stainless steel tube stock (Sandvik) was used for the main body of the pressure vessel. The vendor was chosen as it is known to produce clean stainless steel, and the alloy was chosen for its mechanical properties (yield strength 0.2% = 450 MPa, tensile strength = 680 MPa). The seals were modeled after those used in IceCube’s drill head and were hydrostatically tested to 7000 psi at the University of Wisconsin–Madison Physical Sciences Laboratory (PSL).

Low-background counting was performed at SNO-LAB [41], with results summarized in Table I. This counting included drill water, silicone gel, and excess stock from copper, stainless steel, and PTFE. It was not pos-

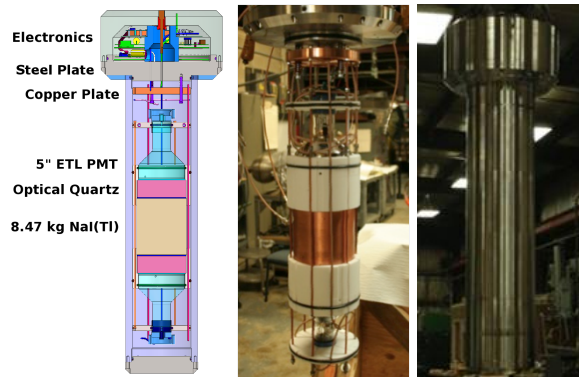


FIG. 1. Engineering drawing (left) and photographs of one of the DM-Ice17 detectors with (right) and without (center) the stainless steel pressure vessel. The wider upper section of the stainless steel vessel contains the digitizing and control electronics, high voltage generation board, and isolation transformer for each PMT. The lower section houses one crystal (light brown in left fig) coupled to two PMTs (light blue) via quartz light guides (pink). Power and communication to the detector is provided through a “special devices” breakout from the main IceCube communication cable. The connection to the detector is made through a single leak-tight penetrator at the top of the pressure vessel.

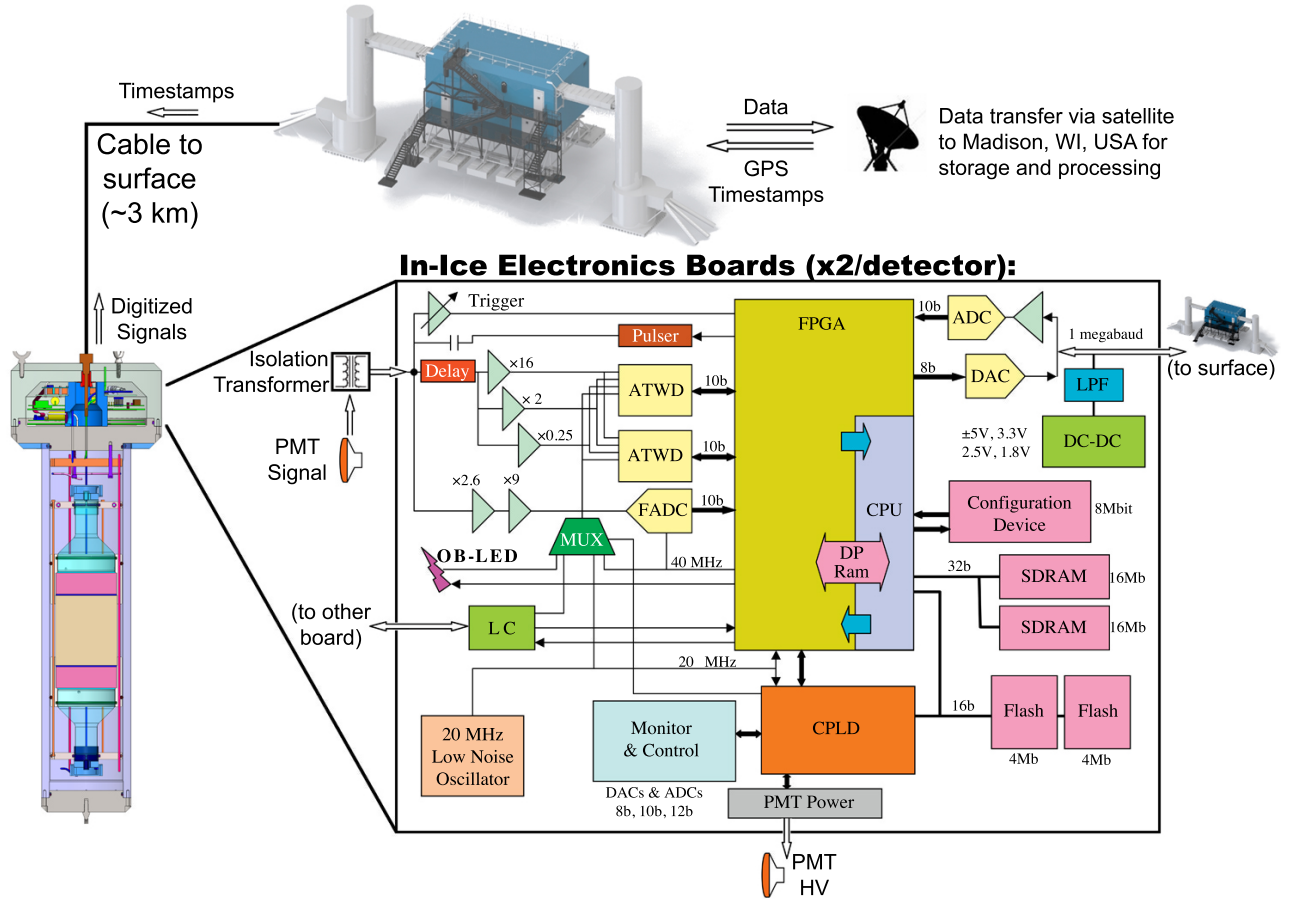


FIG. 2. Block diagram of one DM-Ice17 detector and data transfer. The scintillation light is collected with two PMTs and read out by the two IceCube mainboards (DOM-MBs, described in Ref. [40]) located in the top portion of the pressure vessel. The waveforms are digitized, given a timestamp, and sent to a hub in the ICL through a twisted pair of copper wires. Data are sent via TDRSS satellite to the data warehouse located at the University of Wisconsin–Madison. The DOM-MB is also responsible for controlling the trigger threshold and PMT HV, as well as monitoring relevant PMT and environmental parameters.

sible to screen materials prior to assembly due to the severe time constraints imposed by IceCube’s deployment schedule; therefore, detector components and materials were selected from vendors known to produce radio-clean products. All machined components (e.g. pressure vessel, copper rods, screws) were cleaned using ultrahigh vacuum (UHV) cleaning techniques; the optical components were cleaned with methanol and deionized water. The assembly of detector components was performed in the semiclean room at PSL that was used for assembling IceCube modules.

B. Electronics and DAQ

Each PMT is independently controlled and monitored by its own IceCube digital optical module mainboard (DOM-MB) assembly and high voltage (HV) board [40] located in the top portion of the pressure vessel (see Fig. 2). The DOM-MBs are controlled remotely through a hub located in the IceCube Laboratory (ICL)

on the surface of the ice. The hubs are remotely accessible via TCP/IP when there is a satellite connection to the South Pole Station or by the on-site personnel at any time.

The signal from each PMT is carried on an RG303 cable to the respective DOM-MB. The signal cables have the same length to match their signal transit times. The DOM-MBs contain a field programmable gate array (FPGA) that is configured with a simplified version of IceCube’s data acquisition (DAQ) software [40]. Analog PMT signals passing the trigger conditions are digitized *in situ* by the DOM-MBs before being transmitted to the hub. The hub clock is synchronized to the GPS receiver at the ICL and translates the DOM-MB timestamp into universal time, correcting for the cable lengths of 2500 and 2995 m for Det-1 and Det-2, respectively.

The signal from each PMT is digitized in four separate channels to allow for different time windows and a broad dynamic range. The flash analog to digital converter (FADC) channel collects 255 samples at 40 MHz over a $6.375 \mu\text{s}$ window. The FADC channel has a gain of $\times 23.4$

and 10-bit dynamic range. The three analog transient waveform digitizer (ATWD) channels each collect up to 128 samples at a programmable sampling rate of 100–500 MHz. Each ATWD channel has a 10-bit dynamic range but different gain: “ATWD0” at $\times 16$, “ATWD1” at $\times 2$, and “ATWD2” at $\times 0.25$. Together the ATWD channels offer an effective dynamic range of 14 bits, allowing waveforms to be recorded without saturation from single photoelectrons (sub-keV) up to > 20 MeV.

Although programmable, the run settings were held constant for all physics data presented here. The PMT HV settings were $\{1000, 1000, 1100, 950\}$ V for $\{\text{PMT-1a}, \text{PMT-1b}, \text{PMT-2a}, \text{PMT-2b}\}$. PMT-1a and PMT-1b are the upper and lower PMTs coupled to Det-1 respectively (likewise for PMT-2a and PMT-2b in Det-2). The trigger threshold of each PMT was set to ~ 0.25 photoelectrons. A coincidence window of ~ 400 ns was imposed before recording the waveforms of the two PMTs coupled to the same crystal. The sampling rate of the DM-Ice17 ATWD chips was set at ~ 210 MHz for a digitized waveform time window of ~ 600 ns. A ~ 0.7 ms deadtime is introduced during waveform digitization.

The DAQ records hardware monitoring information including temperature and pressure (measured at the DOM-MB) as well as PMT high voltage and trigger rate. Monitoring information, collected regularly during data taking, was recorded every 2 sec from January 2011 to February 2012 and every 60 sec since then. The monitored parameters are discussed in Sec. III and the associated noise is discussed in Sec. VI.

C. Location

DM-Ice17 is operating in Antarctica roughly 1 km from the geographic South Pole (see Fig. 3). It was codeployed with the final seven strings of IceCube [37] during the construction season of the 2010/2011 austral summer. The two DM-Ice17 detectors were lowered into separate, water-filled holes, each 2457 m deep and 60 cm in diameter, and permanently frozen into place. These holes, drilled by Ice Cube’s enhanced hot water drill, are separated by 545 m. The ice provides 2200 meters water equivalent of overburden.

Both detectors are deployed on IceCube strings, 7 m below the lowest digital optical module (DOM). The IceCube array consists of 1 km^3 of glacial ice instrumented with 5160 DOMs distributed across 86 strings, with 324 additional DOMs on the surface of the ice as IceTop. One of the DM-Ice17 detectors, Det-1, is located near the center of the IceCube array at the bottom of DeepCore [42] on String-79 [43]. Det-2 is at the edge of the IceCube array on String-07. Though operating independently from IceCube, DM-Ice17 uses the same DAQ software and GPS time stamps, providing opportunities to study coincident events with IceCube. The power and communication to the DM-Ice17 detectors are established through twisted pairs of copper wires connected to Ice-

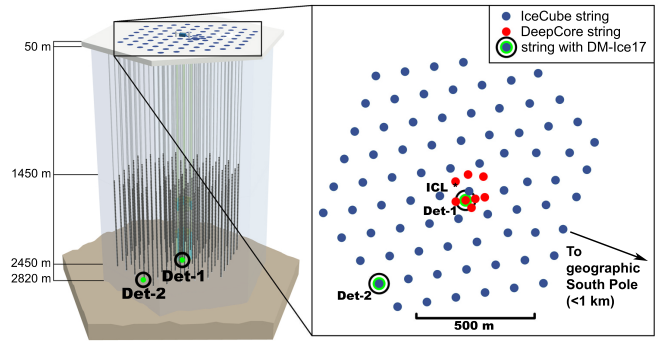


FIG. 3. The locations of the DM-Ice17 detectors within the IceCube array, with Det-1 near the array center and Det-2 at the periphery. Both detectors are at a depth of 2457 m and are horizontally separated by 545 m. In the array top-view, blue points are IceCube strings, and red points are DeepCore strings.

Cube’s main signal cables. They are controlled via hubs in the ICL located on the surface of the ice.

The South Pole ice is 90,000–100,000 years old at depths of 2400–2500 m [44]. This highly pure glacial ice contains ~ 10 ppb of dust, mostly consisting of volcanic ash; the total contamination level from these impurities is $\sim 10^{-5}$ ppb for ^{238}U and ^{232}Th and $\sim 10^{-2}$ ppb for ^{nat}K [45]. Optical scattering measurements made by IceCube precisely quantify the dust concentrations throughout their detector array, allowing the correlation of South Pole ice with Antarctic ice cores. The ^{238}U concentration was validated by the Vostok ice cores using inductively coupled plasma sector field mass spectrometry (ICP-SFMS) [46].

The bedrock’s contribution to the background of the detectors is negligible as they are shielded by over 300 m of ice. The environmental radon is also expected to be a negligible component of the total background as the detectors are completely encased in ice. The contamination levels of the water that fills the drilled holes were measured with HPGe counting. Its simulated contribution to the region of interest for dark matter searches was found to be negligible (see Sec. V A).

III. DETECTOR DEPLOYMENT AND PERFORMANCE

A. Deployment

The detectors were shipped pre-assembled in November 2010, first by land to Los Angeles, CA, then by air to Christchurch, New Zealand. The detectors waited in Christchurch for two weeks on the surface before being flown to McMurdo Station in Antarctica. After a day in McMurdo, the detectors were flown to the South Pole Station. Time spent on the surface at the South Pole (2835 m elevation) was minimized to limit exposure to

the higher cosmic ray rates.

The sealed pressure vessels were strapped down vertically in custom-designed wooden shipping crates. A Shock Timer Plus 3D sensor (Instrumented Sensor Technology) was mounted inside each crate to monitor temperature, humidity, and mechanical shock during shipment. The large mass of the pressure vessel and additional layers of insulation mitigated thermal shock while the suspension system within the pressure vessel dampened mechanical shock to the crystals (see Sec. II A). Bare NaI(Tl) crystals can handle surface temperature gradients of $> 50^\circ\text{C}$ [47], but encapsulated detectors are rated to only 8°C/hr due to different coefficients of thermal expansion of the crystals and encapsulation materials.

From Wisconsin to New Zealand, the temperature varied between 4 and 24°C with a rate of change less than 3°C/hr . Upon arrival at McMurdo Station, the temperature dropped from 25°C to -7°C over 15 hrs. At the South Pole, the temperature dropped 20°C in its first 7 hrs before stabilizing at the surface temperature of roughly -25°C .

Calculations of the thermal conduction of the pressure vessel were made prior to deployment to verify that safe thermal gradients would be experienced at all times, especially during the rapid temperature equilibration upon detector entry into the 0°C water at deployment. The temperature shock was minimized by allowing the detectors to thermalize to 10°C in the deployment tower prior to being lowered rapidly (< 30 min) through the -50°C air column in the top ~ 50 m of the hole.

Thermal variations measured during shipment and storage were $< 6^\circ\text{C/hr}$ prior to detector deployment. The largest mechanical shocks recorded were $< 10g$ for both Det-1 and Det-2 and were primarily during commercial shipment to New Zealand. No damage to the detectors or loss of light collection efficiency can be discerned from the performance of the detectors.

B. Freeze-in and temperature stability

The temperatures of the DOM-MBs are read out as part of the regular monitoring routine (see Fig. 4). The recorded temperatures are $\sim 10^\circ\text{C}$ warmer than the surrounding -18°C ice due to the $\sim 3.5\text{W}$ dissipated by the electronics [40]. The two DOM-MBs in the same pressure vessel are stacked on top of each other and rotated by 60° with respect to one another. The temperature sensor on the top DOM-MB sees a $2-3^\circ\text{C}$ higher temperature than its partner from the dissipated heat of the DC-DC converter located directly below it on the lower DOM-MB.

As the ice froze and the detectors thermalized, the temperature decrease exhibited a fast and a slow exponential time component. The fast freeze-in time constant (~ 10 days) is due to the water in the drilled hole freezing around the detector. The slow component of thermalization (~ 100 days) is thought to be due to the thermaliza-

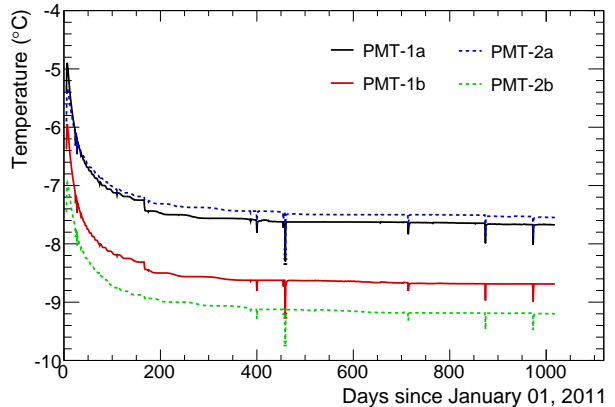


FIG. 4. Temperature recorded by DM-Ice17 mainboards since January 01, 2011, sampled every 2 sec through February 2012 and every 60 sec after (see Sec. II B). Two time constants are observed: a relative fast component (~ 10 days) that relates to the freeze-in process and a slower time constant (~ 100 days) as the heat accumulated in the ice surrounding the hole during drilling is dissipated. Discontinuities observed correspond to the PMT high voltage settings change (day ~ 160) and subsequent power outages (negative spikes).

tion of the heat deposited in the nearby ice during the hot-water drilling process. The small drop on day ~ 160 corresponds to the change in the power dissipation in the mainboard when the PMT high voltage was lowered to the final run settings. The occasional dips in temperature correspond to power outages in either the ICL or the hub affecting the mainboards for more than an hour.

During the two-year physics data run, the temperature of the DM-Ice17 MBs has been stable with a gradual cooling of $\sim 0.25^\circ\text{C}$ and an average daily RMS of $\sim 0.02^\circ\text{C}$. The thermal mass of surrounding ice provides DM-Ice17 with smaller temperature fluctuations than achieved by similar experiments [48]. No temperature modulation is observed within the measurement error. The crystal temperature is expected to be more stable than these DOM-MB measurements due to its larger thermal mass and increased distance from the electronics. The temperature dependence of the detector response is the subject of future studies and is not addressed here.

C. Hardware stability

Regularly recorded PMT high voltages are stable to within fractions of a volt ($0.4-0.8\text{V}_{RMS}$) with the exception of PMT-2b. Despite a constant HV set point, PMT-2b shows random variation in monitored HV around the set point ($\sim 30\text{V}_{pp}$). No correlations are observed between this HV oscillation and either PMT gain or single photoelectron (SPE) rate. The monitored HV is stable to within 0.1mV (1 in 10^4) over the two-year period.

The gain stability of the PMTs was quantified from

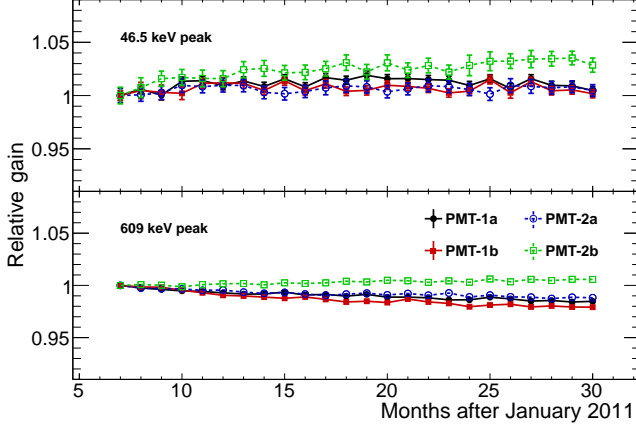


FIG. 5. Relative uncalibrated peak position of the 46.5 keV ^{210}Pb (top) and 609 keV ^{214}Bi (bottom) gamma peaks demonstrating DM-Ice17 gain stability. The 46.5 keV peak has approximately constant light collection, while the 609 keV peak has a $< 2\%$ decrease over two years.

the light collection efficiency at the prominent 609 keV and 46.5 keV peaks in the uncalibrated energy spectrum (see Fig. 5). The 609 keV peak from ^{214}Bi exhibits a small ($< 2\%$) decrease in light collection over two years. The 46.5 keV peak from ^{210}Pb exhibits no significant trend with $< 2\%$ fluctuations. PMT-2b deviates from the trend of the other PMTs at both peaks, showing relative increased gain of a few percent. No time-dependent calibration is applied to the presented data because the gain fluctuations are less than the energy resolution of the detectors; shorter datasets are used for the energy resolution analysis (see Sec. IV C) to limit systematic error of gain drift. No variation is observed in the peak areas within the measurement errors.

The total coincident event rate for each detector is $\sim 2.5\text{ Hz}$ and shows a gradual decrease with time (0.027 Hz/yr for Det-1 and 0.013 Hz/yr for Det-2). No variation with time is observed in the PMT trigger thresholds extracted from dark noise (non-coincident) data runs.

D. Detector lifetime

In the two-year dataset presented here, DM-Ice17 took data nearly continuously, with a total livetime of 98.94% (Det-1) and 98.92% (Det-2). The downtime is primarily from 10 extended (> 1 hour) interruptions due to power outages, test runs, and DAQ errors. Normal uninterrupted data sets achieve a $\sim 99.75\%$ livetime, with small downtime introduced as the DAQ transitions between runs. A $\sim 0.7\text{ ms}$ deadtime after each event ($\sim 2.5\text{ Hz}$ event rate) introduces an additional $\sim 0.18\%$ downtime.

IV. DETECTOR RESPONSE

A. Data processing and calibration

Events passing the trigger threshold and coincidence window requirements are digitized *in situ* by the DOM-MB (see Sec. II B). The digitized waveforms are then sent to the hub in the ICL and compiled into one-hour runs. The data are transmitted via satellite to the University of Wisconsin–Madison for processing.

Offline data processing consists of waveform corrections and energy calibration. The waveform is first baseline adjusted and then corrected for the frequency response of the passive electronic components.

The energy calibration begins by integrating the entire corrected waveform ($\sim 600\text{ ns}$ for ATWD). The resulting spectrum for each PMT is calibrated into keV_{ee} using

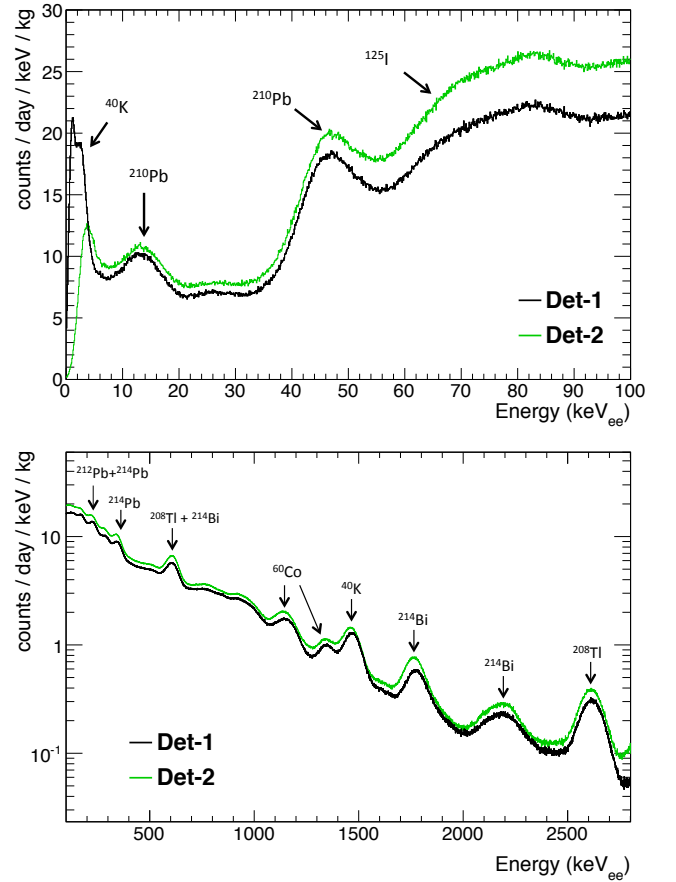


FIG. 6. The calibrated energy spectrum with prominent lines identified for both Det-1 (black) and Det-2 (green). ATWD0 (the highest gain channel) is used for the low-energy plot (top), and ATWD1 is used for the high-energy plot (bottom); the spectra from these two channels overlap well from 100–1000 keV. The nonlinear response of NaI requires that separate calibrations be applied for the two energy regions. All lines depicted are included in calibration fits and energy resolution analysis.

known lines from ^{40}K , ^{60}Co , ^{125}I , ^{232}Th -chain, and ^{238}U -chain. The final energy spectra (see Fig. 6) are produced by combining the light collected in both PMTs on a single crystal for each event. The energies are reported in electron-equivalent keV (keV_{ee}), unless otherwise stated.

The four digitization channels are optimized for different energy ranges based on their gain and saturation energy. ATWD0 is useful for 0–1000 keV, ATWD1 for 100–5000 keV, and ATWD2 >1000 keV. The longer FADC digitization window carries important timing information (see Sec. V C), but the FADC energy spectrum is not used in present analyses.

The nonlinear light response of NaI requires that two different energy calibrations be applied for above and below 100 keV (see Fig. 6). An extrapolation of the high-energy linear calibration results in a negative intercept, consistent with behavior observed in literature [49, 50].

B. Cosmogenic isotopes

Cosmogenically activated isotopes are produced in the detector components prior to deployment and provide a robust verification of the energy calibration. The activation rates were simulated in ACTIVIA (NaI crystal) [51] or obtained from literature values (steel pressure vessel) [52]. The activation calculation incorporates the duration of the stages of construction, shipment, and deployment, as well as the rate scaling for each geographic location and elevation. The resulting isotopes were propagated through the detector using the DM-Ice17 GEANT4 simulation package (see Sec. V A). In DM-Ice17 data, ^{125}I from ^{127}I activated in the crystal and ^{54}Mn from ^{56}Fe in the pressure vessel provide the clearest cosmogenic signals due to their energies and half-lives.

Cosmogenic ^{125}I is observed (see Fig. 7), exhibiting the expected peaks at 37.7 and 65.3 keV resulting from a combination of gammas and X-rays. Using one-month intervals of data, the measured half-life of this isotope is 59.4 ± 2.7 days, consistent with the quoted 59.40 ± 0.01 day half-life of ^{125}I [53]. The ^{125}I activity, extrapolated back to deployment, was determined to be 1150 ± 120 decays/day/kg. Simulation using ACTIVIA estimated an activity of 410 decays/day/kg. This discrepancy is within the error of the ACTIVIA activation rate [51] and scaling factor calculations.

The gamma line from ^{54}Mn at 836.1 ± 3.0 keV is also observed (see Fig. 7), consistent with the literature value of 834.848 ± 0.003 keV [53]. The measured half-life is consistent with the tabulated value of 312 days, although precise measurement has not been made due to low statistics. The ^{54}Mn activity, extrapolated back to deployment assuming the literature half-life, was determined to be 51700 ± 6500 decays/day (corrected for detection efficiency of decays in the pressure vessel found from GEANT4 simulation). Simulation based on literature activation rates estimated an activity of 41850 ± 4650 decays/day (error only from activation rate

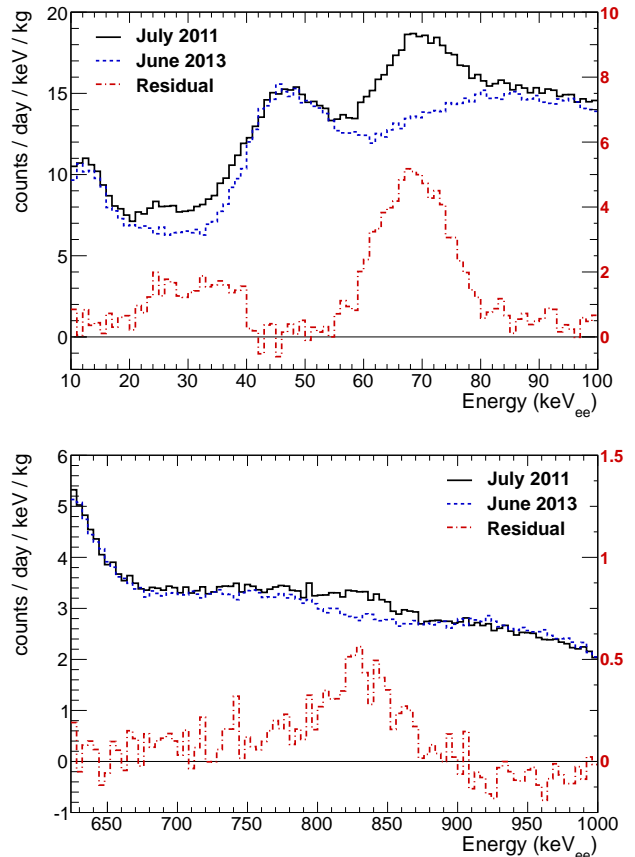


FIG. 7. Det-1 spectra from July 2011 (black, solid), June 2013 (blue, dashed), and residual (red, dot-dashed, on rescaled axis) showing evidence for cosmogenic activation. The top figure shows the decay of the 37.7 and 65.3 keV lines from cosmogenic ^{125}I in the crystal. The bottom figure shows the decay of the 834.8 keV gamma line from cosmogenic ^{54}Mn in the pressure vessel.

measurement) from the pressure vessel, in good agreement given additional uncertainty in the scaling factors.

C. Energy resolution and light yield

The energy resolution of the DM-Ice17 detectors (see Fig. 8) is measured by fitting a Gaussian plus linear background to the prominent peaks from internal contamination. The resolution measured in the DM-Ice17 detectors is comparable to that of similarly sized NaI detectors from ANAIS-25 [54], DAMA/LIBRA [55], and NaIAD [38], as well as to that of a small $2 \times 1 \times 1 \text{ cm}^3$ NaI crystal [56]. The resolution of the 3 keV peak from ^{40}K has large error due to the uncertainty in the cut efficiency (see Sec. VI). The ~ 14 keV peak from ^{210}Pb is broadened due to the many (>10) X-rays that make up that peak. The 2204 keV peak from ^{214}Bi is broadened by contributions from ^{208}Tl decay.

Single photoelectron (SPE) events are collected by re-

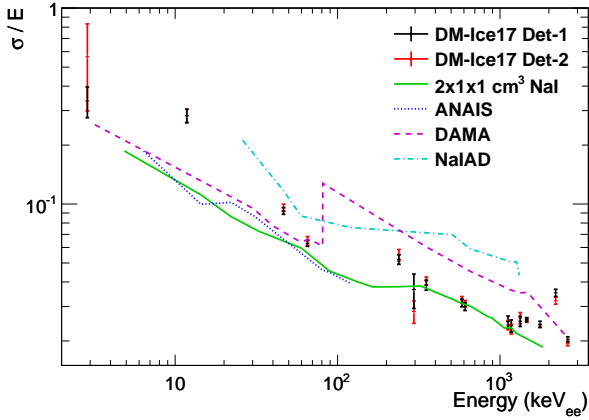


FIG. 8. Energy resolution of Det-1 (black) and Det-2 (red) compared to ANAIS-25 (blue, dotted) [54], DAMA/LIBRA (magenta, dashed) [55], NaIAD detector DM77 (cyan, dot-dashed) [38], and a $2\times 1\times 1\text{ cm}^3$ NaI detector (green, solid) [56]. The discontinuity in the DAMA resolution is due to switching ADC channels at $\sim 80\text{ keV}$. The internal contamination lines were fit with a Gaussian plus linear background, the quantity σ is the fitted standard deviation and the error bar is the fitted parameter error.

moving the two-PMT coincidence trigger requirement during regularly scheduled dark noise runs. The light yield is measured by comparing the peak location of the 65.3 keV calibration line from ^{125}I to that of the SPE peak. The measured light yields are $5.9 \pm 0.1\text{ pe/keV}$ and $4.3 \pm 0.1\text{ pe/keV}$ for Det-1 and Det-2 respectively.

D. Pulse shape discrimination for alphas

Alpha events can be separated from gammas via pulse shape discrimination. Alphas produce shorter scintillation waveforms than gammas, leading to observable differences in the behavior in the tail of the recorded waveforms [55, 57]. A comparison of average alpha and gamma waveforms, as recorded in the ATWD1 channel, is shown in Fig. 9. Longer time windows are available in the FADC channel; however, the pulses are saturated for MeV events and therefore are not used in this analysis.

A parameter referred to as the mean time (τ) quantifies the decay behavior of waveforms and is defined numerically as

$$\tau = \frac{\sum_{n=n_0}^{n_0+99} (n - n_0) (ADC_n)}{\sum_{n=n_0}^{n_0+99} ADC_n},$$

where ADC_n refers to the charge collected in the n th time bin of the waveform and n_0 is the time when the waveform first reached 50% of its maximum. To account for variations in the time between the start of scintillation and the start of the recorded waveform, the mean

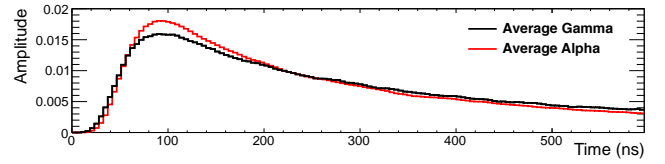


FIG. 9. An average of 100 normalized gamma and alpha waveforms as recorded in the ATWD1 channel of PMT-1a. Particle identification is possible through pulse-shape discrimination.

time calculation begins at n_0 and samples 100 bins. The separation observed (see Fig. 10) using the mean time parameter is consistent with that reported by other NaI(Tl) experiments [55, 58], although our shorter sampling window reduces the calculated mean time.

Above 2000 keV_{ee} , gamma and alpha separation via the mean time nears 100%. These two bands can be accurately represented by Gaussian functions with nonoverlapping tails; in the $2500\text{--}3500\text{ keV}_{ee}$ region, less than one misidentified event is expected for the 24 months of data presented here.

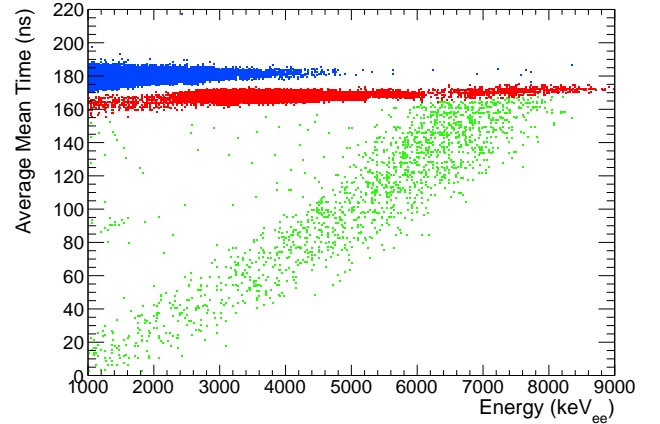


FIG. 10. Waveform mean time values from Det-1 demonstrating separation between electron recoils (blue, $\tau \approx 180\text{ ns}$) and alpha events (red, $\tau \approx 165\text{ ns}$). The diagonal band at lower τ (green) is composed of Bi-Po events (see Sec. VC).

V. BACKGROUND ANALYSIS

A. External backgrounds

The energy spectrum over $100\text{--}3000\text{ keV}$ from the DM-Ice17 data shows good agreement with simulations based on radioassays of components and data-based estimates (see Fig. 11). The background levels of the two detectors are comparable, and the spectrum from Det-1 is shown as representative of the two. The contamination levels used in the simulation are listed in Table II for the NaI crystals and in Table I for all other components.

TABLE I. Contamination levels of DM-Ice17 detector components in mBq/kg. Quartz measurements are from ILIAS database for ‘Spectrosil B silica rod’ [59], and PMT levels are from the low-background ETL 9390B datasheet (with increased ^{238}U). Components that were measured specifically for this experiment at SNOLAB [41] are indicated by *. Components not shown in Fig. 11 are indicated by † .

Material	^{40}K	^{232}Th	^{238}U (^{234}Th)	^{238}U (^{226}Ra)	^{235}U	^{60}Co
Quartz Light Guides	0.50 ± 0.03	< 4.9		12
ETL 9390B PMT	9300	1000		2400
Steel Pressure Vessel *	13.77 ± 6.38	6.49 ± 0.96	118.31 ± 60.11	2.28 ± 0.72	8.79 ± 1.68	7.19 ± 0.82
Drill Ice *	3.71 ± 1.36	0.55 ± 0.17	6.69 ± 3.02	0.39 ± 0.14	0.38 ± 0.21	0.12 ± 0.05
Silicone Optical Gel * †	39.50 ± 18.60	< 0.12	2.08 ± 1.10	38.50 ± 61.00	0.96 ± 1.30	0.32 ± 0.42
PTFE Supports * †	0.34 ± 5.09	0.52 ± 0.44	< 0.41	24.46 ± 21.37	1.92 ± 0.72	< 0.089
Copper Plate * †	< 5.13	< 1.22	0.17 ± 0.92	< 0.67	3.56 ± 1.79	< 0.12
Glacial Ice †	$\sim 3 \times 10^{-4}$	$\sim 4 \times 10^{-4}$	$\sim 10^{-4}$	

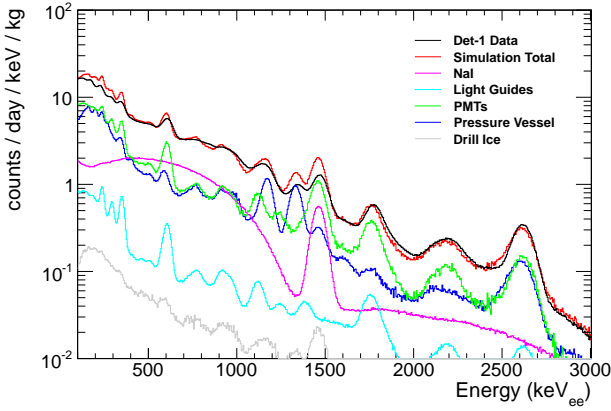


FIG. 11. The beta/gamma energy spectrum in keV_{ee} from Det-1 (black) and comparison to simulation (red). The simulated contributions of significant detector components are shown separately. Simulated contaminant levels are derived from data-based estimates and radioassays (see Table I and Table II).

During construction, excess stock from the stainless steel pressure vessel, PTFE supports, and copper plate, as well as the silicone gel used for optical coupling, were set aside to be measured at SNOLAB’s low-background counting facility [41]. Samples of the drill water were taken just prior to heating and recirculation. Eleven water samples were taken at varying depths on eight separate holes. The contamination levels measured in the extracted drill water show no significant dependence on the depth or the order in which the holes were drilled; Table I shows the average measured contamination.

The contamination levels for the quartz light guides were taken from the ‘Spectrosil B silica rod’ values on the ILIAS database [59]. The contamination levels for the low-background ETL 9390 PMTs were provided in the vendor data sheet; the ^{238}U -chain level was increased by 95% to better match data. The contamination levels

of the NaI crystals were derived from spectral features in data validated by simulation (see Sec. VB). The PTFE light reflector and copper enclosing the crystal (Saint-Gobain encapsulation) were simulated with bulk contamination levels matching the newer materials (PTFE supports and OFHC copper plate measured at SNOLAB); a surface contamination (0–10 μm) in the copper of 40 mBq of ^{238}U -chain was included to better match data (see Sec. VI). The glacial ice contamination is estimated using dust impurity levels measured by Ice-Cube [44] scaled to appropriate contamination levels [45] (see Sec. II C and [36]). The contributions from contamination in the PTFE supports, copper rods and plate, silicone optical gel, quartz light guides, drill ice, and glacial ice were simulated and found to be insignificant.

Detector and background modeling were performed using the 4.9.5 release of the GEANT4 software package [60, 61]. The physics list utilizes the standard electromagnetic interaction models with atomic relaxation [62] as demonstrated in the “rdecay02” example code.

B. Backgrounds from NaI crystals

The alpha lines between 4.0 and 7.5 MeV were used to measure the ^{238}U and ^{232}Th contaminations in the NaI(Tl) crystals. The events in these lines are expected to be dominated by those occurring in the bulk of the NaI(Tl) crystals. The spectrum from each PMT is compared to the GEANT4-based simulation and contamination levels are evaluated from the respective peak areas (see Fig. 12). Both ^{238}U - and ^{232}Th -chains appear to be broken, as described in Table II. The cause of the shoulders observed in the peaks of the alpha spectrum is under investigation.

The scintillation yield of the NaI(Tl) detectors is lower for alpha than for gamma interactions. The measured alpha quenching factors are $\alpha/\gamma = 0.435 + 0.039E_\alpha(\text{MeV})$ and $\alpha/\gamma = 0.47 + 0.034E_\alpha(\text{MeV})$ for Det-1 and Det-2, respectively, consistent with those reported in [55].

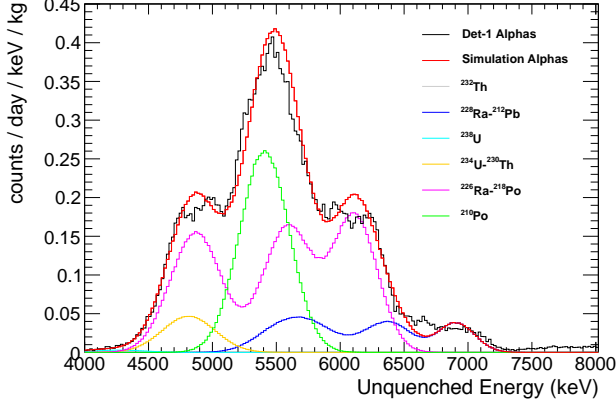


FIG. 12. The energy spectrum in the alpha region of ^{238}U and ^{232}Th and chains in the NaI(Tl) crystal as measured with PMT-1b of Det-1 (black) and simulation (red). Comparison to simulation yields contaminant level estimates of the ^{238}U - and ^{232}Th -chains in the crystal (see Table II). The energy scale shown takes into account the correction from the gamma-calibrated spectrum using the quenching factor (see text).

TABLE II. Contamination in the DM-Ice17 NaI crystals as determined by simulation comparison to data spectral features. The activity levels in the two detectors are consistent within the $\sim 30\%$ error of these numbers. Both ^{238}U - and ^{232}Th -chains were observed to be broken.

Isotope	Subchain	Activity (mBq/kg)
^{40}K		17
^{129}I		1
^{232}Th	^{232}Th	0.01
	$^{228}\text{Ra}-^{208}\text{Tl}$	0.16
^{238}U	$^{238}\text{U}-^{234}\text{Pa}$	0.017
	$^{234}\text{U}-^{230}\text{Th}$	0.14
	$^{226}\text{Ra}-^{214}\text{Po}$	0.90
	$^{210}\text{Pb}-^{210}\text{Po}$	1.5

For short-lived isotopes ^{214}Po (^{238}U -chain) and ^{212}Po (^{232}Th -chain), activities are estimated by Bi-Po events from data (see Sec. V C). This analysis supports the contamination levels derived from the alpha spectrum.

The contamination levels of ^{40}K and ^{129}I were measured by using their continuous beta spectra with endpoints at 1311 keV and 154 keV, respectively, to match the simulation with the data.

C. Bi-Po events

For short-lived isotopes in a decay chain, it is possible to observe parent and daughter decays in a single recorded waveform (see Fig. 13). For the ~ 600 ns

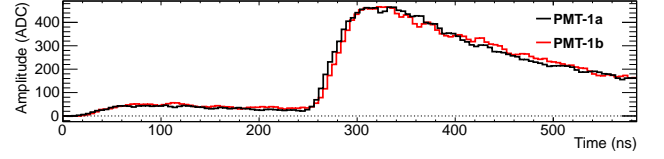


FIG. 13. An example Bi-Po waveform recorded in the ATWD1 channels of PMT-1a (black) and PMT-1b (red). The first peak is the beta decay from ^{212}Bi , and the second larger peak is from the alpha decay of ^{212}Po ($t_{1/2} = 299$ ns).

sample window of DM-Ice17, this most commonly occurs for the ^{232}Th -chain decays $^{212}\text{Bi} \rightarrow ^{212}\text{Po} \rightarrow ^{208}\text{Pb}$ (^{212}Po $t_{1/2} = 299 \pm 2$ ns [53]). A secondary contribution to the double-event population comes from the ^{238}U -chain decays $^{214}\text{Bi} \rightarrow ^{214}\text{Po} \rightarrow ^{210}\text{Pb}$ (^{214}Po $t_{1/2} = 164.3 \pm 0.2$ μs [53]).

Because the high-energy alpha event is delayed, a larger portion of the waveform tail is truncated. This loss results in a correlated suppression of the calculated mean time and calibrated energy of these events (see Fig. 10).

The time between the two energy depositions in the waveform yields a distribution dominated by the exponential component due to ^{212}Bi over the approximately flat continuum due to ^{214}Bi (see Fig. 14). The exponential component of the fit yields a half-life of 298.6 ± 4.0 ns, consistent with ^{212}Po being the source of these events.

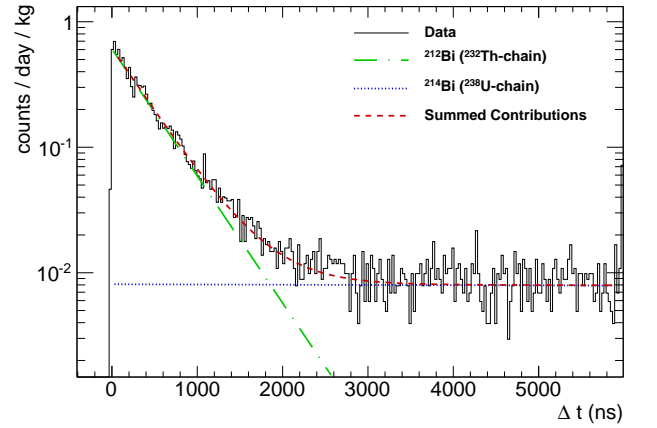


FIG. 14. The time between gamma and subsequent alpha decay of Bi-Po events in PMT-1a. Exponential fit component from ^{212}Bi decay (green, dot-dashed), flat continuum from ^{214}Bi decay (blue, dotted), and composite fit (red, dashed) are overlain on data (black, solid).

This analysis and the simulation comparison to the alpha peaks (see Sec. V B) yield similar results for the levels of contamination observed in the NaI crystals (see Table III).

TABLE III. Contamination levels of ^{212}Bi (^{232}Th -chain) and ^{214}Bi (^{238}U -chain) in the DM-Ice17 NaI crystals derived from Bi-Po data analysis and simulation. These values are consistent within the $\sim 30\%$ error of the simulation estimates.

Isotope	Bi-Po Analysis ($\mu\text{Bq/kg}$)		Simulation ($\mu\text{Bq/kg}$)
	Det-1	Det-2	
^{212}Bi	176 ± 6	173 ± 6	160
^{214}Bi	930 ± 12	955 ± 12	900

VI. LOW ENERGY REGION

The energy spectrum below 25 keV is shown in Fig. 15. The raw spectrum (shown in solid black line) below 20 keV is dominated by three noise components: electromagnetic interference (EMI), thin pulses, and correlated single photoelectrons (SPE) between the two PMTs. The distinctive pulse shape of each event type is used to identify the noise; the spectrum after cuts is shown in gray. Thin pulses are the dominant noise source in the region of interest (2–20 keV), while EMI and SPE noise dominate below 1 keV. The waveforms associated with signal and these sources of noise are shown in Fig. 16.

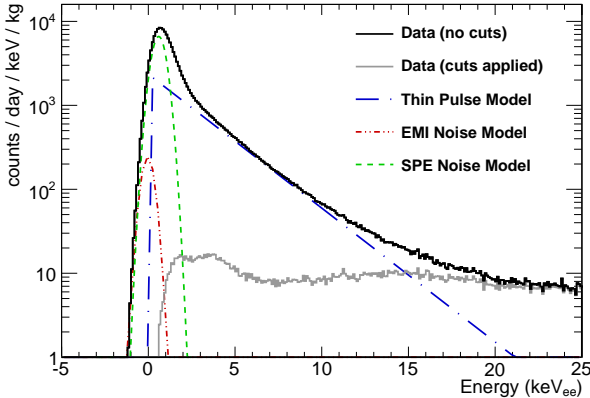


FIG. 15. The low energy spectrum of Det-1 before (black, solid) and after (gray, solid) analysis cuts. Models of the noise from thin pulses (blue, dot-dashed), electromagnetic interference (red, dot-dot-dashed), and correlated single photoelectrons (green, dashed) are shown.

EMI events occur when the mainboards are queried for their monitoring information (see Sec. II B). These events are characterized by their oscillatory waveforms (see Fig. 16(d)), which can be distinguished from signal events by summing the square of the second derivative. This EMI cut parameter is

$$\sum_n \left[(ADC_{n+1} - ADC_n) - (ADC_n - ADC_{n-1}) \right]^2,$$

where ADC_n is the n th time bin in the recorded waveform. Removal of EMI events is 99.98% efficient while

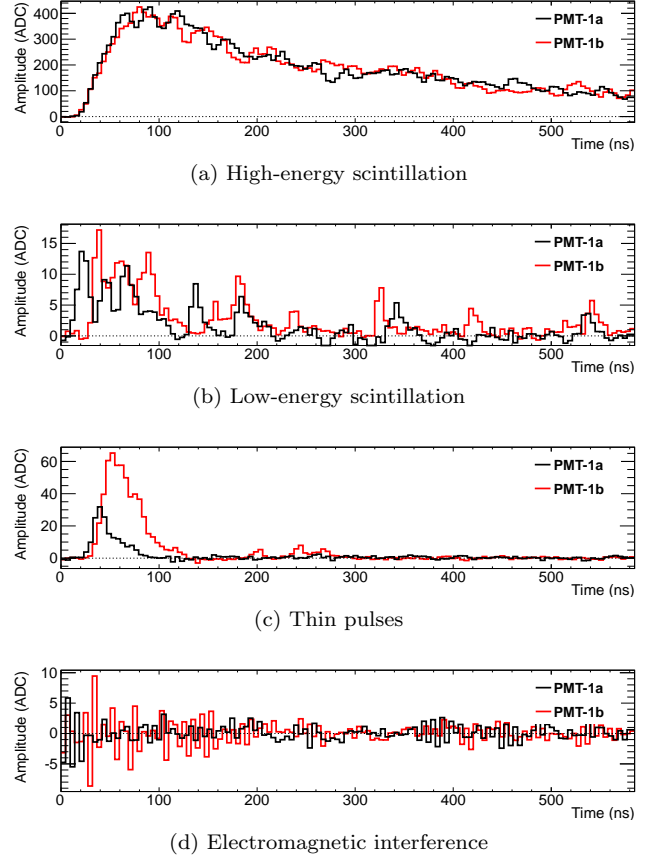


FIG. 16. Example coincident waveforms of different event types recorded by PMT-1a (black) and PMT-1b (red). Waveforms (a) and (b) are signal events at high (700 keV) and low (7 keV) energies, respectively. Waveforms (c) and (d) are thin pulse (9 keV) and EMI (0.2 keV) noise events removed from raw data by cuts.

preserving 99.99% of low energy non-EMI events. The calibrated energy of EMI events is centered at 0 keV; the highest energy observed is at 1.6 keV. The monitoring query interval was increased from 2 to 60 sec in February 2012, significantly reducing the number of EMI triggers.

Thin pulse events are characterized by tall, narrow waveforms and asymmetric energy deposition in the two PMTs (see Fig. 16(c)). Most of the light is collected within 100 ns, a much faster decay time than that of NaI scintillation (~ 300 ns in DM-Ice17 data). Above 4 keV, thin pulse and scintillation event populations are well resolved using the ratio of the pulse area to the pulse height. The energy spectrum of thin pulses from 4–20 keV is exponential, and is modeled to persist back to 0 keV (see Fig. 15). Thin pulses are suspected to originate from interactions in the quartz or PMT windows [55, 63]. Their timing characteristics are similar to noise pulses observed in other NaI detectors including those of DAMA/LIBRA [55]. Understanding their stability and contribution to the signal region is critical for annual modulation studies.

Correlated SPE noise events form a Gaussian peak with a mean of 0.6 keV and a standard deviation of 0.4 keV (see green dashed line in Fig. 15). The shape matches the SPE spectrum observed in non-coincident characterization runs, but the rate is two orders of magnitude higher than expected from random coincidences between uncorrelated single photoelectrons from the two PMTs. The ~ 100 Hz SPE rates should produce ~ 0.01 Hz of accidental coincidences inside the 400 ns coincidence window, but the observed rate of correlated SPE noise events is ~ 1 Hz.

Both thin pulse and SPE events are removed from the data set by cutting on the number of “peaks” (local maxima) observed in the recorded waveform. Low-energy scintillation events (see Fig. 16(b)) are composed of multiple photoelectrons (5.9 and 4.3 pe/keV for Det-1 and Det-2, respectively; see Sec. IV C), whereas thin pulse and SPE events typically only contain one peak. The cut efficiency can be analyzed down to 4 keV using pulse shapes, at which energy the signal passing efficiency is 60% with signal to noise ratio of 16. The cut efficiency below 4 keV is a topic of ongoing investigation.

Several low energy features are visible in the data after applying cuts: a broad peak around 14 keV, a peak at 3 keV, and remnant noise below 2 keV. These features are reproduced by GEANT4 simulations (see Fig. 17). The broad peak at 14 keV can be attributed mostly to surface contamination of the ^{238}U -chain in the copper encapsulation (40 mBq from the inner 10 μm); surface contamination of this type has been observed previously in other NaI(Tl) experiments [64]. The 3 keV peak is from Auger electrons and X-rays from ^{40}K decays in the crystal. The flat background of the crystal out to 30 keV is dominated by contributions from ^{210}Pb (^{238}U -chain) and ^{40}K .

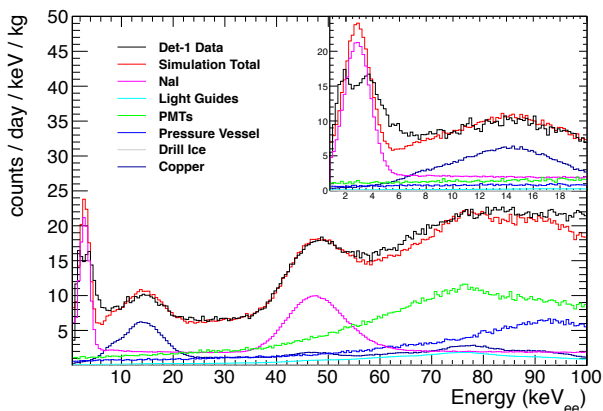


FIG. 17. The energy spectrum of DM-Ice17 Det-1 (black) and simulation total (red). Simulated contributions from nearby detector components are also shown. The spectrum below 20 keV consists primarily of the 3 keV peak from ^{40}K and a 14 keV peak from ^{238}U -chain decays on the surface of the copper encapsulation. The background observed between 6.5–8 keV is 7.9 ± 0.4 counts/day/keV/kg.

A background of 7.9 ± 0.4 counts/day/keV/kg is observed between 6.5–8 keV, below which the spectrum is dominated by the ^{40}K peak. DAMA/LIBRA reports a single-hit spectrum with 0.9 counts/day/keV/kg background level after application of a multi-crystal anti-coincidence veto [55]. Recently grown crystals being tested by ANAIS [54] and KIMS [58] have achieved a background level of 3–4 counts/day/keV/kg after cuts.

VII. CONCLUSIONS

DM-Ice17 was successfully constructed and deployed in December 2010. The data presented here from July 2011 – June 2013 demonstrate the excellent environmental conditions, including temperature stability with daily RMS of 0.02°C. A livetime of $\sim 99\%$ was achieved by the detectors during this period.

It has been shown for the first time that low-background scintillator detectors can be remotely calibrated and operated under the ice at the South Pole. This has promising implications for future dark matter searches in the Southern Hemisphere.

The background observed in DM-Ice17 is in good agreement with simulation of expected contaminants levels in detector components; contributions from backgrounds in the environmental ice have been shown to be negligible. Below 20 keV, the spectrum is dominated by contributions from the crystals and encapsulation; in the 6.5–8.0 keV region, a rate of 7.9 ± 0.4 counts/day/keV/kg is observed, consistent with expected backgrounds. The energy region of interest between 2 and 6 keV is dominated by the events from ^{40}K peak at 3 keV. An active research and development program toward achieving lower contaminant levels, particularly of ^{40}K and ^{238}U -chain, is currently underway. The backgrounds observed in new DM-Ice crystals as well as DM-Ice17 analyses of the low-energy region, muon coincidence with IceCube, and cosmogenic activation will be discussed in separate papers.

ACKNOWLEDGMENTS

We thank the IceCube Collaboration and construction team for their support in the successful deployment of the detector and on-going detector monitoring and data management. We thank the support from SNOLAB for their efforts on the low-background measurements, and STFC and the Boulby mine company CPL for support of low-background measurements of NaI. This work was supported by the NSF Grants No. PLR-1046816 and No. PHY-1151795, Wisconsin IceCube Particle Astrophysics Center, the Wisconsin Alumni Research Foundation, Yale University, the Natural Sciences and Engineering Research Council of Canada, and Fermilab, operated by Fermi Research Alliance, LLC under Contract No. DE-AC02-07CH11359 with the United States De-

partment of Energy. W. P. and A. H. are supported by the DOE/NSA Stewardship Science Graduate Fellow-

ship (Grant No. DE-FC52-08NA28752) and NSF Graduate Research Fellowship (Grant No. DGE-1256259), respectively.

-
- [1] P. Ade *et al.* (Planck Collaboration), *Astron. Astrophys.* **571**, A17 (2014), [arXiv:1303.5076 \[astro-ph.CO\]](#).
 - [2] G. Bertone, D. Hooper, and J. Silk, *Phys. Rep.* **405**, 279 (2005), [arXiv:hep-ph/0404175 \[hep-ph\]](#).
 - [3] S. Faber and J. Gallagher, *Annu. Rev. Astron. Astrophys.* **17**, 135 (1979).
 - [4] G. Steigman and M. S. Turner, *Nucl. Phys.* **B253**, 375 (1985).
 - [5] P. Cushman *et al.*, in *Community Summer Study 2013: Snowmass on the Mississippi. (CSS2013)* (2013) [arXiv:1310.8327 \[hep-ex\]](#).
 - [6] M. W. Goodman and E. Witten, *Phys. Rev. D* **31**, 3059 (1985).
 - [7] A. Drukier, K. Freese, and D. Spergel, *Phys. Rev. D* **33**, 3495 (1986).
 - [8] K. Freese, J. A. Frieman, and A. Gould, *Phys. Rev. D* **37**, 3388 (1988).
 - [9] S. Chang, A. Pierce, and N. Weiner, *J. Cosmol. Astropart. Phys.* **01**, 006 (2010), [arXiv:0908.3192 \[hep-ph\]](#).
 - [10] R. Bernabei *et al.*, *Int. J. Mod. Phys. D* **13**, 2127 (2004), [arXiv:astro-ph/0501412 \[astro-ph\]](#).
 - [11] R. Bernabei *et al.*, *Eur. Phys. J. C* **73**, 2648 (2013), [arXiv:1308.5109 \[astro-ph.GA\]](#).
 - [12] C. Aalseth *et al.* (CoGeNT Collaboration), *Phys. Rev. D* **88**, 012002 (2013), [arXiv:1208.5737 \[astro-ph.CO\]](#).
 - [13] C. Aalseth *et al.* (CoGeNT Collaboration), “Search for an Annual Modulation in Three Years of CoGeNT Dark Matter Detector Data,” (2014), [arXiv:1401.3295 \[astro-ph.CO\]](#).
 - [14] G. Angloher *et al.* (CRESST Collaboration), *Eur. Phys. J. C* **72**, 1971 (2012), [arXiv:1109.0702 \[astro-ph.CO\]](#).
 - [15] R. Agnese *et al.* (CDMS Collaboration), *Phys. Rev. Lett.* **111**, 251301 (2013), [arXiv:1304.4279 \[hep-ex\]](#).
 - [16] R. Agnese *et al.* (SuperCDMS Collaboration), *Phys. Rev. Lett.* **112**, 241302 (2014), [arXiv:1402.7137 \[hep-ex\]](#).
 - [17] D. Akerib *et al.* (LUX Collaboration), *Phys. Rev. Lett.* **112**, 091303 (2014), [arXiv:1310.8214 \[astro-ph.CO\]](#).
 - [18] G. Angloher *et al.* (CRESST-II Collaboration), “Results on Low Mass WIMPs Using an Upgraded CRESST-II Detector,” (2014), in preparation, [arXiv:1407.3146 \[astro-ph.CO\]](#).
 - [19] E. Aprile *et al.* (XENON100 Collaboration), *Phys. Rev. Lett.* **109**, 181301 (2012), [arXiv:1207.5988 \[astro-ph.CO\]](#).
 - [20] S. Kim *et al.* (KIMS Collaboration), *Phys. Rev. Lett.* **108**, 181301 (2012), [arXiv:1204.2646 \[astro-ph.CO\]](#).
 - [21] E. Aprile *et al.* (XENON100 Collaboration), *Phys. Rev. Lett.* **111**, 021301 (2013), [arXiv:1301.6620 \[astro-ph.CO\]](#).
 - [22] S. Archambault *et al.* (PICASSO Collaboration), *Phys. Lett. B* **711**, 153 (2012), [arXiv:1202.1240 \[hep-ex\]](#).
 - [23] E. Behnke *et al.* (COUPP Collaboration), *Phys. Rev. D* **86**, 052001 (2012), [arXiv:1204.3094 \[astro-ph.CO\]](#).
 - [24] M. Felizardo *et al.* (SIMPLE Collaboration), *Phys. Rev. Lett.* **108**, 201302 (2012), [arXiv:1106.3014 \[astro-ph.CO\]](#).
 - [25] A. V. Belikov, J. F. Gunion, D. Hooper, and T. M. Tait, *Phys. Lett. B* **705**, 82 (2011), [arXiv:1009.0549 \[hep-ph\]](#).
 - [26] P. Draper, T. Liu, C. E. Wagner, L.-T. Wang, and H. Zhang, *Phys. Rev. Lett.* **106**, 121805 (2011), [arXiv:1009.3963 \[hep-ph\]](#).
 - [27] M. R. Buckley, D. Hooper, and T. M. Tait, *Phys. Lett. B* **702**, 216 (2011), [arXiv:1011.1499 \[hep-ph\]](#).
 - [28] M. I. Gresham and K. M. Zurek, *Phys. Rev. D* **89**, 016017 (2014), [arXiv:1311.2082 \[hep-ph\]](#).
 - [29] D. Hooper, J. Collar, J. Hall, D. McKinsey, and C. Kelso, *Phys. Rev.* **82**, 123509 (2010), [arXiv:1007.1005 \[hep-ph\]](#).
 - [30] D. Nygren, “A Testable Conventional Hypothesis for the DAMA-LIBRA Annual Modulation,” (2011), [arXiv:1102.0815 \[astro-ph.IM\]](#).
 - [31] K. Blum, “DAMA vs. the Annually Modulated Muon Background,” (2011), [arXiv:1110.0857 \[astro-ph.HE\]](#).
 - [32] J. H. Davis, *Phys. Rev. Lett.* **113**, 081302 (2014), [arXiv:1407.1052 \[hep-ph\]](#).
 - [33] J. P. Ralston, “One Model Explains DAMA/LIBRA, CoGeNT, CDMS, and XENON,” (2010), [arXiv:1006.5255 \[hep-ph\]](#).
 - [34] P. J. Fox, J. Liu, and N. Weiner, *Phys. Rev. D* **83**, 103514 (2011), [arXiv:1011.1915 \[hep-ph\]](#).
 - [35] S. K. Lee, M. Lisanti, A. H. G. Peter, and B. R. Safdi, *Phys. Rev. Lett.* **112**, 011301 (2014), [arXiv:1308.1953 \[astro-ph.CO\]](#).
 - [36] J. Cherwinka *et al.*, *Astropart. Phys.* **35**, 749 (2012), [arXiv:arXiv:1106.1156 \[astro-ph.HE\]](#).
 - [37] A. Achterberg *et al.* (IceCube Collaboration), *Astropart. Phys.* **26**, 155 (2006), [arXiv:astro-ph/0604450 \[astro-ph\]](#).
 - [38] B. Ahmed *et al.*, *Astropart. Phys.* **19**, 691 (2003), [arXiv:hep-ex/0301039 \[hep-ex\]](#).
 - [39] G. Alner *et al.* (UK Dark Matter Collaboration), *Phys. Lett. B* **616**, 17 (2005), [arXiv:hep-ex/0504031 \[hep-ex\]](#).
 - [40] R. Abbasi *et al.* (IceCube Collaboration), *Nucl. Instrum. Methods Phys. Res., Sect. A* **601**, 294 (2009), [arXiv:arXiv:0810.4930 \[physics.ins-det\]](#).
 - [41] I. Lawson and B. Cleveland, *AIP Conf. Proc.* **1338**, 68 (2011).
 - [42] R. Abbasi *et al.* (IceCube Collaboration), *Astropart. Phys.* **35**, 615 (2012), [arXiv:1109.6096 \[astro-ph.IM\]](#).
 - [43] T. K. Gaisser, *Adv. Space Res.* **51**, 242 (2013), [arXiv:1107.1690 \[astro-ph\]](#).
 - [44] M. Ackermann *et al.* (IceCube Collaboration), *J. Glaciology* **59**, 1117 (2013).
 - [45] W. I. Rose and T. J. Bornhorst, *AAPG Special Volumes* **SG 13**, 13 (1981).
 - [46] P. Gabrielli *et al.*, *Earth Planet. Sci. Lett.* **234**, 249 (2005).
 - [47] K. Forrest, C. Haehner, T. Heslin, M. Magida, J. Uber, S. Freiman, G. Hicho, and R. Polvani, NASA STI/Recon Technical Report N **84**, 33613 (1984).
 - [48] R. Bernabei *et al.* (DAMA Collaboration), *Eur. Phys. J. C* **56**, 333 (2008), [arXiv:0804.2741 \[astro-ph\]](#).
 - [49] D. Engelke, *Rev. Sci. Instrum.* **27**, 589 (1956).
 - [50] I. Khodyuk, P. Rodnyi, and P. Dorenbos, *J. Appl. Phys.* **107**, 113513 (2010), [arXiv:1102.3799 \[physics.ins-det\]](#).
 - [51] J. Back and Y. Ramachers, *Nucl. Instrum. Methods Phys. Res., Sect. A* **586**, 286 (2008), [arXiv:0709.3472](#)

- [52] M. Laubenstein and G. Heusser, *Appl. Radiat. Isot.* **67**, 750 (2009).
[\[nucl-ex\]](#).
- [53] B. N. L. National Nuclear Data Center, “Nudat (nuclear structure and decay data),” (2008).
- [54] J. Amaré *et al.*, *Nucl. Instrum. Methods Phys. Res., Sect. A* **742**, 187 (2014), [arXiv:1308.3478 \[physics.ins-det\]](#).
- [55] R. Bernabei *et al.* (DAMA Collaboration), *Nucl. Instrum. Methods Phys. Res., Sect. A* **592**, 297 (2008), [arXiv:0804.2738 \[astro-ph\]](#).
- [56] E. Sakai, *IEEE Trans. Nucl. Sci.* **34**, 418 (1987).
- [57] C. Cuesta *et al.*, *Opt. Mater.* **36**, 316 (2013), [arXiv:1307.1398 \[astro-ph.IM\]](#).
- [58] K. Kim *et al.*, *Astropart. Phys.* **62**, 249 (2015), [arXiv:1407.1586 \[astro-ph.IM\]](#).
- [59] ILIAS, “Database on radiopurity of materials,” (2007).
- [60] S. Agostinelli *et al.*, *Nucl. Instrum. Methods Phys. Res., Sect. A* **506**, 250 (2003).
- [61] J. Allison *et al.*, *IEEE Trans. Nucl. Sci.* **53**, 270 (2006).
- [62] S. Guatelli, A. Mantero, B. Mascialino, P. Nieminen, and M. Pia, *IEEE Trans. Nucl. Sci.* **54**, 585 (2007).
- [63] J. Amaré *et al.*, *Opt. Mater.* **36**, 1408 (2014), [arXiv:1401.3118 \[physics.optics\]](#).
- [64] S. Cebrián *et al.*, *Astropart. Phys.* **37**, 60 (2012).